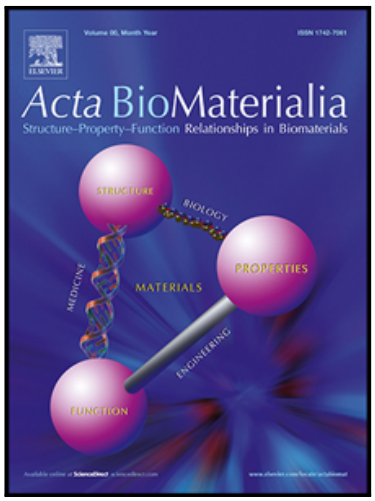

Biomimetic and Hierarchical Nerve Conduits from Multifunctional Nanofibers for Guided Peripheral Nerve Regeneration

Juan Wang , Yuan Cheng , Haoyu Wang , Yuhao Wang , Kuihua Zhang , Cunyi Fan , Hongjun Wang , Xiumei Mo

PII: S1742-7061(20)30560-2
DOI: https://doi.org/10.1016/j.actbio.2020.09.037
Reference: ACTBIO 6952

To appear in: *Acta Biomaterialia*

Received date: 2 May 2020
Revised date: 17 September 2020
Accepted date: 22 September 2020

Please cite this article as: Juan Wang , Yuan Cheng , Haoyu Wang , Yuhao Wang , Kuihua Zhang , Cunyi Fan , Hongjun Wang , Xiumei Mo , Biomimetic and Hierarchical Nerve Conduits from Multifunctional Nanofibers for Guided Peripheral Nerve Regeneration, *Acta Biomaterialia* (2020), doi: https://doi.org/10.1016/j.actbio.2020.09.037

Biomimetic and Hierarchical Nerve Conduits from Multifunctional Nanofibers for Guided Peripheral Nerve Regeneration

Juan Wang [a, c, d], *Yuan Cheng* [b], *Haoyu Wang* [d], *Yuhao Wang* [d], *Kuihua Zhang* [e], *Cunyi Fan* [b], *Hongjun Wang* [d, *], *Xiumei Mo* [a, *]

[a] *State Key Laboratory for Modification of Chemical Fibers and Polymer Materials College of Chemistry, Chemical Engineering and Biotechnology, Donghua University, Shanghai 201620, China*

[b] *Department of Orthopaedics, Shanghai Jiao Tong University Affiliated Sixth People's Hospital, Shanghai, China*

[c] *Shanghai Key Laboratory for Prevention and Treatment of Bone and Joint Diseases Shanghai Institute of Traumatology and Orthopaedics Ruijin Hospital Shanghai Jiao Tong University School of Medicine, Shanghai, China*

[d] *Department of Biomedical Engineering, Stevens Institute of Technology, Hoboken, New Jersey 07030, USA*

[e] *College of Materials and Textile Engineering, Jiaxing University, Jiaxing, Zhejiang, China*

***** To whom correspondence should be addressed. Tel: 021-67792653, Fax: 021-67792653. E -mail: xmm@dhu.edu.cn; hwang2@stevens.edu

ABSTRACT

Development of a functional nerve conduit to replace autografts remains a significant challenge particularly considering the compositional complexity and structural hierarchy of native peripheral nerves. In the present study, a multiscale strategy was adopted to fabricate 3D biomimetic nerve conduit from *Antheraea pernyi* silk fibroin (*Ap*F)/(Poly(L-lactic acid-co-caprolactone)) (PLCL)/graphene oxide (GO) (*Ap*F/PLCL/GO) nanofibers *via* nanofiber dispersion,

template-molding, freeze-drying and crosslinking. The resultant conduits exhibit parallel multichannels (ϕ = 125 μm) surrounded by biomimetic fibrous fragments with tailored degradation rate and improved mechanical properties in comparison with the scaffold without GO. *In vitro* studies showed that such 3D biomimetic nerve scaffolds had the ability to offer an effective guiding interface for neuronal cell growth. Furthermore, these conduits showed a similarity to autografts in *in vivo* repairing sciatic nerve defects based on a series of analysis (walking track, triceps weight, morphogenesis, vascularization, axonal regrowth and myelination). The conduits almost completely degraded within 12 weeks. These findings demonstrate that the 3D hierarchical nerve guidance conduit (NGC) with fascicle-like structure have great potential for peripheral nerve repair.

Keywords

Biomimetic nanofibrous fragments; 3D mutichannels sponges; angiogenesis; nerve repair

1. Introduction

Peripheral nerve regeneration and functional recovery have been a major clinical challenge, especially for those long-distance nerve defects, which typically require the bridging by nerve grafts [1]. Autografts are regarded as the “gold standard” for nerve injury in clinical surgery. However, the inherent drawbacks such as limited donor sources, donor site morbidity and additional surgery procedures constrain their wide use [2, 3]. In recognition, extensive efforts have been made to develop nerve guidance conduits (NGCs), enabling guided cell growth and axon extension to promote peripheral nerve regeneration and function restoration [4].

The initial NGC design adopts a single hollow tube configuration to support cell attachment and facilitate axon extension of injured neural tissues. However, such simple hollow NGCs often cause the dispersion of axons and consequently lead to inappropriate targeted reinnervation or

polyinnervation [5-7]. In recognition, efforts have been made to introduce filling materials (*e.g.*, gels, sponges, filaments, and fibers) into the NGC lumen for topological cues to guide nerve regeneration [8-11]. Reduced permeability of such a configuration, however, significantly limits axon ingrowth. In parallel, efforts have also been extended towards more complex design, *i.e.*, closely mimicking the morphology and functions of native nerve tissues [12-14]. As such, the basic structure of to-date NGCs also comprises of multiple intraluminal channels [5, 6, 15] to prevent the dispersion of regenerated axons [16]. However, the current multichannelled NGCs suffer from poor mechanical flexibility and small cross-sectional area of channel, unfavorable for axon ingrowth [17, 18]. Thus, it remains highly desirable to develop a biomimetic NGC with maximal recapitulation of the native nerve-growing environment for accelerated and guided axon growth to achieve better functional integration.

Notably, the myelinated and unmyelinated axons of peripheral nerve are encased by endoneurium, mainly composed of collagen fibers, to form the fascicles [19]. Recapitulation of such morphological and structural uniqueness of fascicles in NGCs would offer neural cells with supportive cues and therefore promote neurogenesis [20]. Electrospinning, a simple yet versatile technology, has demonstrated its ability to produce nanofibers with great dimensional similarity to natural collagen fibers [21-23]. However, these electrospun matrices typically exhibit as dense fibrous laminae with the inter-fiber distance less than 5 μm, which is not conducive to cell ingrowth [24] and not able to recapitulate the spatial organization of perineurium fibers. In recognition, recent endeavors have been extended to further process the electrospun fibers to yield three dimensional (3D) structures, *e.g.*, the formation of porous sponge *via* thermal-induced self-agglomeration of fragmented electrospun fibers followed by freeze-drying [25] or *via* freeze-drying of a suspension of fragmented electrospun fibers followed by heat-induced cross-linking [26]. Following the later

approach, Sun *et al.* explored the possibility of fabricating NGC out of 3D nanofiber sponges [27]. While improving the pore size and porosity, the irregular pores, random pore distribution, and uncontrollable interconnectivity of the sponges are not desirable for nerve regeneration, especially considering the limited mass exchange for nutrition transport and constrained migration of Schwann cells (SCs) for axon ingrowth. To address these challenges in conjunction with the attempt to mimic the native microenvironment of peripheral nerves, we therefore introduced parallel multichannels into the 3D fibrous sponges to develop biomimetic NGCs with perineurium-like structure. Cumulative evidence has also highlighted the essence of physicochemical properties (*e.g.*, stiffness, biodegradability and surface chemistry) of NGCs in regulating the development of myelinated axons [28]. Such properties are normally correlated with the materials used. In view of the distinct advantages of respective natural and synthetic materials, herein, a promising composite of *Antheraea pernyi* silk fibroin (*Ap*F)/(poly(L-lactic acid-co-caprolactone)) (PLCL) was particularly selected to achieve the bioactivities and preferred flexibility [29, 30]. In addition, recent attention has also been given to graphene oxide (GO) - an oxidized derivative of graphene, for its demonstrated biocompatibility, elevated mechanical properties and promoted proliferation and differentiation of neural cells [31-33]. In this regard, GO was also blended into *Ap*F/PLCL to formulate three-component composite nanofibers in anticipation of further improving the capability of guiding nerve regeneration.

In this study, a hierarchical, multifunctional and biomimetic NGC was designed in such a way to yield an intimate setting of perineurium by mimicking the fascicle-like architecture and axial orientation of nerve tissues. Based on *Ap*F/PLCL/GO nanofibers, the multichannel sponge-containing NGC (MCS-NGC) was fabricated *via* the combination of nanofiber dispersion, template-molding, freeze-drying and crosslinking as shown in Figure 1a. The physicochemical

properties of MCS-NGCs such as morphology, mechanical properties, and degradation were characterized. Proliferation, infiltration and myelination (myelin-specific gene expression and neurotrophic factor secretions) of SCs on the MCS-NGC were studied *in vitro* and its ability to guide nerve regeneration was also investigated using the sciatic nerve defect model of rats.

2. Materials and methods

2.1. Materials

Poly (L-lactic acid-co-caprolactone) PLCL (LA/CL=50/50) was purchased from Jinan Daigang Bioengineering Co. Ltd (Jinan, China). Chinese tussah silkworm *A. pernyi* silk cocoons were purchased from Liaoning province (China). Graphene oxide (GO) was provided by Nanjing XFNANO Materials Tech Co., Ltd. (Nanjing, China). 1, 1, 1, 3, 3, 3-Hexafluoro-2-propanol (HFIP) was obtained from Shanghai Co., Ltd. (China). The cells were supplied by Shanghai Institute of Biochemistry and Cell Biology (China). Cell culture reagents were acquired from Gibco (UK). All other chemicals of reagent grade were obtained from Shanghai Aladdin Bio-Chem Technology Co., Ltd. (China).

2.2. Preparation and characterization of GO-incorporated electrospun ApF/PLCL nanofibers

The regenerated *Ap*F was prepared as previously reported [34]. The *Ap*F/PLCL polyblend solution (10 wt%) was prepared by dissolving *Ap*F and PLCL at a weight ratio of 4:1 in HFIP, and then 2 wt% GO (the mass ratio of GO to GO+PLCL+*Ap*F) was added into the solution and stirred to obtain a homogeneous solution. The optimal electrospinning conditions for *Ap*F/PLCL/GO nanofibers were determined: the flow rate, the applied voltage, and the collection distance were set at 1.5 mL/h, 12 kV, and 10 cm, respectively. The relevant temperature and humidity during

electrospinning were 25 ± 2°C and 45 ± 2%, respectively. The prepared *Ap*F/PLCL/GO nanofiber meshes were vacuum dried to remove trace solvent. Morphology of the electrospun meshes was examined by scanning electron microscopy (SEM, HITACHI TM-100, Japan). The average nanofiber diameter was determined by analyzing randomly selected fibers (at least 100) of the SEM micrographs using Image J. The distribution of GO in *Ap*F/PLCL nanofibers was further investigated by transmission electron microscopy (TEM, JEOL, JEM-2100, Japan). Wettability of the electrospun nanofiber meshes was determined by measuring the apparent contact angle using a contact angle analyzer (OCA40, Dataphysics, Germany). These nanofibers were also respectively characterized with a Fourier transform infrared (FTIR, Nicolet Nexus 670 FTIR spectrometer) and Raman spectrometer (Via-Reflex Renishaw plc, England).

2.3. Fabrication and characterization of 3D ApF/PLCL/GO MCS

As illustrated in **Figure 1a**, the preparation of 3D MCS involved three key steps: (1) cutting of *Ap*F/PLCL/GO nanofibers into small fragments; (2) dispersion of the small fragments in tert-butanol by homogenizing with IKA T-18 at 10,000 rpm for 30 min; (3) the dispersions were poured into the multichannel mold (diameter: 2 mm; channel number: 30; channel spacing: 50 μm), frozen in liquid nitrogen for 1 h and then freeze dried for 48 h to obtain the uncrosslinked scaffolds. To stabilize the structure, 3D MCS was further crosslinked with the glutaraldehyde vapor for 20 min, and then immersed in 5% glutamate-hydrochloric acid solution for 12 h to remove residual glutaraldehyde.

Morphology of the scaffolds was examined by SEM. The porosity (%) of 3D MCS was evaluated *via* liquid displacement. Briefly, each scaffold in a dry state was weighed and placed in absolute acetone for 48 h. The porosity was then calculated as previously reported [35] and average porosity

was obtained from five different measurements. Channel size was determined by Image J analysis. The mechanical properties of MCS in the wet state, and the relevant media and temperature were deionized water and 25 ± 2°C, respectively. were evaluated by cyclic compression testing using a material testing machine (HY-940FS, China).

2.4. Biodegradation of 3D MCS

Degradation of MCS is closely regulated by the cross-linking degree, which is proportional to the cross-linking time. To further confirm this correlation, MCS scaffolds were crosslinked with glutaraldehyde vapor for 0, 10, 20, 40, and 60 min, respectively. The relative changes of β-sheet in the fractional contents of 3D MCS over different crosslinking times were determined based on the FTIR spectra using Origin 8.5 analysis software. Briefly, to measure different conformations, average spectrum in the amide I mode was deconvoluted and curve fitted (1587-1725 cm^{-1}). Curve fitting was modulated using the Gaussian model by the autofit program using initially local least-squares followed by Levenberg-Marquardt algorithms. Fixed band widths were initially selected based on the deconvoluted spectra to obtain conformational positions of amide I regions. Finally, each individual spectrum areas were normalized to obtain percentage conformations within the amide I region. The procedure was repeated three times. Degradation of the cross-linked MCS scaffolds was monitored by weight loss. Briefly, the scaffolds were incubated at 37°C in phosphate buffered saline (PBS) solution (pH 7.4) and the solution was refreshed every 2 days. At the designated time points, the scaffolds were centrifuged at 10,000 rpm for 5 min and washed with deionized water. Upon freeze-drying, the remaining weight was recorded and compared to the initial weight.

2.5. Proliferation and infiltration of SCs on scaffolds

To evaluate the supportiveness of MCS for nerve cells, SCs (1.0×10^4 cells/well) were seeded on the scaffolds placed in 48-well plates with 600 μL culture mediums for each well and cultured for 1, 3, 5 and 7 day. *Ap*F/PLCL/GO nanofiber meshes were used as controls. Cell proliferation was determined by MTT assay. The morphology of SCs on *Ap*F/PLCL/GO nanofiber meshes and MCS after 7-day culture was examined by immunofluorescence staining, hematoxylin & eosin (H&E) staining, and SEM. Briefly, cultured SCs were fixed with 4% paraformaldehyde at 4°C and dehydrated in a series of ethanol solution. Part of the dehydrated samples was dried using CO_2 critical point dryer and sputter-coated with gold for SEM examination. The rest of the dehydrated samples were embedded in paraffin and then cut into thin sections across the center. The thin sections were conducted for H&E or immunofluorescence staining. The stained slides were examined with a confocal laser scanning microscope (CLSM, C2, Nikon, Japan) to analyze the SCs infiltration.

2.6. qRT-PCR, Western blot，flow cytometry and NGF secretion assay

Myelination of SCs cultured on 3D MCS was evaluated by qRT-PCR, flow cytometry and western blot. *Ap*F/PLCL/GO nanofiber meshes were used as controls. Gene expression of neuronal cellular adhesion molecules (NCAM), nerve growth factor (NGF), peripheral myelin protein 22 (PMP22) and early growth response 2 (Krox20) were examined by real-time PCR after culture for 7 days. Corresponding primer sequences are listed in Table S1, and gene expression were analyzed *via* the $2^{-\triangle\triangle Ct}$ method. Protein level of NCAM and NGF was determined by Western blot as previously reported [36]. For flow cytometry analysis, the cells cultured for 7 days were fixed with 80% methanol and permeabilized with Triton X-100 for 20 min. The cells were then incubated with 10% normal goat serum to block non-specific protein-protein interactions followed by antibody

incubation (NCAM and NGF) for 30 min at 22°C. After gentle washing, the cells were incubated with secondary antibody (goat anti-rabbit IgG conjugated with Alexa Fluor 488 at a dilution of 1/4000) for 30 min at 22°C. For each sample, 1×10^4 cells were counted and all experiments were repeated at least three times. The acquired data were analyzed with WinMDI2.9 software. To determine NGF secreted by SCs into media, the supernatant of culture media was collected and analyzed with the NGF ELISA kit following the manufacturer's instruction (Boster, China)

2.7. PC12 cell differentiation

The bioactivity of growth factors secreted by SCs on *Ap*F/PLCL/GO nanofiber meshes and MCS was evaluated based on PC12 cell differentiation. Briefly, PC12 cells (1.0 x 10^4 cells/well) were seeded into well plates and incubated for 24 h. Then the media was replaced with conditioned media collected from SCs cultured on nanofibers or MCS and supplemented with 2.5% FBS. The culture with normal PC12 medium was used as negative controls (NM group), and that with normal PC12 medium but supplemented with 10 ng/mL NGF was used as positive controls (NM+NGF group). Differentiation of PC12 cells was assessed by immunofluorescence staining. Briefly, the cultured cells were respectively incubated with anti-beta III tubulin antibody (1:100, Abcam, USA) and fluorescein-conjugated goat anti-rabbit IgG (1:200, Abcam, USA). The stained cells were examined with an epifluorescence microscope (H600L, Nikon, Japan) for cell morphology and neurite outgrowth. The neurite length and percentage of differentiated cells were determined as previously reported [30].

2.8. Preparation of 3D MCS-NGC

To obviate the infiltration of fibrous scar tissue that hinders axonal regeneration and promote nerve regeneration *in vivo*, MCS were made into conduits as illustrated in **Figure 4a**. Briefly, (1)

the MCS was placed as a filler between two parallel positioned permanent magnets; (2) *Ap*F/PLCL nanofiber was warped on the surface of MCS by magnetic electrospinning to obtain MCS NGC (2 mm (ϕ) × 10 mm (L)). During magnetic electrospinning, the magnetic field drives the electrospinning fibers parallel to the magnetic field lines, finally the fibers laid on MCS scaffolds between two magnets. The relevant temperature and humidity during electrospinning were 25 ± 2°C and 45 ± 2%, respectively. Electrospun *Ap*F/PLCL nanofiber tubes (2 mm (ϕ) × 10 mm (L)) without MCS filler named as Hollow-NGC were used as controls.

2.9. Animal Implantation

All surgery procedures were performed according to the standard Institutional Animal Care guidelines. Healthy male Sprague-Dawley (SD) rats (200-250g in weight) were used to evaluate the nerve repair capacity of as-prepared nerve conduits and autografts. Briefly, sciatic nerve defects of 10 mm were created on the SD rats and then bridged with corresponding nerve conduits. For autografts group, the excised nerve was re-bridged back to nerve stumps. The rats were randomly divided into 3 groups: Hollow-NGC, MCS-NGC and autografts. All the rats were sacrificed at 12 weeks after surgery.

2.10. Morphogenesis and angiogenesis of regenerated nerves

For morphological analysis, the middle segments of regenerated nerves were fixed with 4% paraformaldehyde, embedded in paraffin and cut into thin sections. The sections were stained with hematoxylin and eosin (H&E), toluidine blue (TB) and luxol fast blue (LFB) and then examined under a light microscope. Positively stained cells and myelin were recorded and analyzed by Image J. The axon diameter and myelin thickness of regenerated nerves were detected with a TEM (JEOL, JEM-2100, Japan) and calculated using Image J as described previously [27].

Considering the importance of vascularization for SC migration and peripheral nerve regeneration, cross-sections of the regenerated nerves were immunofluorescently stained by CD34 to visualize the microvessel formation. Briefly, thin sections of the middle segments of regenerated nerves were respectively incubated with rabbit anti-CD34 primary antibody (1:100, Abcam, USA) and secondary antibodies FITC-labeled goat anti-rabbit IgG (1:200, Abcam). The stained sections were examined under the epifluorescence microscopy and the microvessel density was calculated by Image J analysis.

2.11. Axonal regrowth and nerve myelination of regenerated nerves

Immunohistochemistry and immunofluorescence staining were preformed to evaluate nerve regeneration. Thin sections of the regenerated nerves were immunohistochemically stained following the incubation with primary antibody for mouse anti-glial fibrillary acidic protein (GFAP, Abcam), and then peroxidase-conjugated secondary antibody (goat anti-mouse IgG H&L (HRP (1:200, Abcam)). The stained specimens were observed with a light microscope and recorded for analysis using Image J. For immunofluorescence staining, the sections were incubated with primary antibody for S-100 or NF-200, followed by secondary antibody (FITC- or TRITC- conjugated goat anti-rabbit IgG (1:200, Abcam)). Cell nuclei were stained with DAPI (1:200, Life Technologies). The stained sections were examined with an epifluorescence microscope and recorded for analysis using Image J.

2.12. Functional analysis of regenerated nerves

To evaluate the functional recovery of the regenerated sciatic nerve, walking track analysis and triceps weight analysis were performed. For walking track analysis, the hind limbs of the rats were painted with red ink and the footprints were collected when the rats walked on the white paper. Toe

spread length (TS), paw length (PL), and intermediary toe spread (IT) were measured for both experimental (E) and normal legs (N). The sciatic function index (SFI) was calculated as follows [37]:

$$SFI=109.5(ETS-NTS)/NTS-38.3(EPL-NPL)/NPL+13.3(EIT-NIT)/NIT - 8.8 \quad \text{Equation (1)}$$

For triceps weight analysis, the triceps surae muscle (TSM) of each side of legs were carefully dissected out and weighed. The TSM weight percentage was calculated as below:

$$TSM\ weight\ ratio\ (\%) = TSM\ (experimental\ leg)/TSM\ (normal\ leg) \quad \text{Equation (2)}$$

The TSMs were stained with Masson trichrome and the percentage of collagen was estimated using Image J.

2.13. Statistical analysis

All data were presented as means ± SD. Statistical analysis was performed by One-Way ANOVA to evaluate the significant differences among experimental groups. $P < 0.05$ and $P < 0.01$ were considered significant and highly significant, respectively.

3. Results

3.1. Preparation and characterization of GO-containing MCS

3D MCS with parallel microchannels was prepared following the key procedures as illustrated in **Figure 1a**: electrospinning to fabricate nanofibers; fragmentation and dispersion of nanofibers; pouring of fragmented nanofiber suspension into the multichannel mold; freeze-drying and cross-linking. Polyblend solutions of *Ap*F/PLCL or *Ap*F/PLCL/GO were electrospun into fibers following a similar setup as reported [29]. Electrospun *Ap*F/PLCL and GO-incorporated *Ap*F/PLCL

nanofibers both exhibited as randomly oriented nonwoven mats (**Figure S1a-d**). TEM examination of GO-incorporated nanofibers showed the presence of GO nanoflakes on the fiber surface (**Figure S1f**), different from the relatively smooth surface of *Ap*F/PLCL only fibers (**Figure S1e**). In addition, incorporation of GO into *Ap*F/PLCL did lead to the decrease of mean diameter from 499 to 198 nm, which may result from the change of the electrospinning solution by GO [38]. The presence of two characteristic bands D (1352 cm^{-1}) and G (1590 cm^{-1}) of GO in the Raman spectra of *Ap*F/PLCL/GO fiber mats (**Figure S1g**) [39] confirmed successful incorporation of GO into *Ap*F/PLCL nanofibers. Further FTIR analysis revealed that the spectra of *Ap*F/PLCL/GO fiber mats (**Figure S1h**) was simply a combination of *Ap*F/PLCL and GO spectra and no additional signature peaks were observed, suggesting that the existence of GO in *Ap*F/PLCL nanofibers was solely physical mixing without chemical reaction. To determine the distribution of GO in GO-incorporated nanofibers, surface chemistry of fibers was characterized by the high-resolution XPS spectra of C1s. The peaks at 284.6, 286.0, 287.1 and 288.5eV (**Figure S1i**) correspond to C-C/C=C, C-O-C/C-OH, C=O, and HO-C=O bands, respectively [40]. The peak area ratios between oxygen-containing functional groups to C-C/C=C peak, as well as the atomic percentage of carbon, oxygen, nitrogen and atomic ratio of O/C, were calculated. Clearly, the peak area ratios of *Ap*F/PLCL fibers were consistently higher than those of GO-incorporated *Ap*F/PLCL ones (**Figure S1j-k**). Meanwhile, the atomic percentage of C and O, and the O/C ratio of GO-incorporated nanofibers were also slightly higher than those of *Ap*F/PLCL fibers. These results suggest that more GO might be located at the surface of nanofibers. Besides, GO-incorporated *Ap*F/PLCL nanofibers also showed better hydrophilicity compared to *Ap*F/PLCL nanofibers, consistent with the findings from others [38]. The improved hydrophilicity most likely comes from the oxygen active groups (COOH, OH and C-O-C groups) of GO and this helped the fragmentation and dispersion. Following the established

protocol [26], GO-incorporated nanofibers were fragmented into short pieces and then used to fabricate the MCS. As shown in **Figure 1d**, microchannels (ϕ = 125 μm) were evenly distributed across MCS along the axial direction, which resulted in a high porosity (99.7 %) with the channel size as large as 125 μm (**Figure 1h & i**). Close examination by SEM revealed well-reserved fibrous structure of fragmented GO-incorporated nanofibers in the resultant MCS (**Figure 1g**). As a matter of fact, such a hierarchical organization represents a great similarity to the architecture of nerve fascicles [19], beneficial for cell migration and nutrition supply. In addition, the mechanical properties of MCS were also evaluated. As shown in **Figure 1j**, MCS exhibited good compression recovery capacity even after compression for 100 times. A maximum stress of 0.76 MPa was achieved at the first cycle and dropped to 0.66 MPa after 100 cycles. A similar trend was seen with the Young's modulus, decreasing from 0.034 MPa (first cycle) to 0.017 MPa (after 100 cycles). Although the scaffold without GO showed similar good compression recovery capacity after 100-time compression, the maximum stress of the scaffold without GO showed 7 times lower than that of the MCS with GO, and the Young's modulus of the scaffold without GO was around 2 times lower than that of the MCS with GO since the first cycle or even after 100-time compression (**Figure 1j** & **Figure S1l**).

To investigate the effect of crosslinking time on the degradation of MCS, scaffolds were crosslinked with glutaraldehyde vapor for designated duration (0, 10, 20, 40, and 60 min). FTIR spectra were accordingly obtained to monitor the changes of the secondary structure of *Ap*F. As shown in **Figure S2a**, uncrosslinked scaffolds (0 min) had the absorption bands at 1655 cm^{-1}, assigned to the α-helix and random coil conformation [34], The absorption band gradually decreased with the increase of crosslinking time. In contrast, significant absorbance peaks at 1630 cm^{-1} appeared after 20-min crosslinking and became pronounced over the extension of crosslinking

time. This absorption band is characteristic of β-sheet structure, confirming the conformational transformation from a random α-helix coil into a β-sheet. A correlation between the crosslinking time and β-sheet structure of *Ap*F was established by calculating the percentage of β-sheet based on the experimental curves (**Figure S2b**). As shown in **Figure S2c**, the amount of β-sheet structures continuously increased over the crosslinking time, but reached its plateau by 40 min, indicating the secondary structure transformation is near its completion. Previous study showed that *Ap*F degradation was greatly affected by β-sheet formation [41]. In this study, we found that higher β-sheet content could slow down the *Ap*F degradation rate (**Figure S2d**). Thus, the *Ap*F degradation could be tuned *via* cross-linking time. For subsequent studies, scaffolds with a 20-min crosslinking time were used for their intermediate degradation rate.

3.2. Proliferation and myelination of SCs on MCS

To determine the supportiveness of MCSs for cell proliferation, SCs were cultured in the MCS and compared to 2D nanofiber meshes (control). Both nanofiber mesh and MCS supported continuous proliferation of SCs, but a markedly higher number of cells on MCS were measured after 5 days (**Figure 2a**). Different from nanofiber mesh, on which SCs attached and spread as monolayer (**Figure 2b**), MCS supported the attachment and growth of SCs mainly along the luminal surface of microchannels, but also partially inside the fragmented nanofiber matrix as confirmed by both H&E and fluorescence staining of the cross-sections (**Figure 2c**). These results suggest that MCS not only supports cell proliferation but also guides cell infiltration and spatial distribution. SEM examination also confirmed even distribution of round SCs on the luminal surface of microchannels. The sample examination showed the presence of new ECM fibrous network formation (arrowheads in **Figure 2c**) around the SCs, distinct from the underneath

fragmented GO-*Ap*F/PLCL fibers in terms of fiber diameters.

Aside from proliferation, SC myelination is essential to support the peripheral nerve regeneration [42]. SCs cultured on MCS or nanofiber mesh for 7 days were evaluated for their myelination. Quantification of gene expression for several key markers (NCAM, NGF, PMP22 and Krox20) using qRT-PCR revealed that the gene level of NGF, PMP22 and Krox20 on MCS was significantly higher compared to that on the nanofiber meshes (**Figure 3a**), while NCAM, a promyelination marker and only expressed in immature SCs, was much lower, implying the onset of SC myelination [42]. Western blotting and flow cytometry analysis further confirmed a higher NGF and lower NCAM protein levels for SCs cultured on MCS than any other substrates (**Figure 3b-e**). These results demonstrate the benefits of MCS in SC myelination. In addition, myelinating SCs usually up-regulate myelin genes and release neurotrophins, relevant to peripheral nerve regeneration [43]. Among various neurotrophins, NGF is considered the most potent one, stimulating neuronal differentiation and axonal outgrowth [44]. Detection of NGF in the culture media by ELISA revealed that SCs cultured on MCS constantly secreted more NGF and the difference became even more pronounced after 3 days (**Figure 3f**). The bioactivity of secreted NGF was further evaluated with PC12 cells, which could differentiate into neuron-like cells with the presence of NGF. As shown in **Figure 3g**, PC12 cells cultured with MCS conditioned media for 5 days exhibited a comparable level of differentiation to that of NM (normal media) + NGF group and higher than NM group or the culture with nanofiber conditioned media. Quantification of the percentage of differentiated PC12 cells and the average neurite length further confirmed this observation (**Figure 3h-i**). These results illustrate that MCS would promote axonal growth for peripheral nerve regeneration by neurotrophins secreted by SCs.

3.3. Preparation of MCS-NGC for sciatic nerve regeneration

To determine whether MCS could promote nerve regeneration *in vivo*, MCS-NGC was accordingly fabricated by electrospinning a layer of *Ap*F/PLCL nanofibers in axial orientation onto MCS (**Figure 4a**). The final NGC has an outer diameter of 2 mm and a length of 10 mm. Hollow tubes of *Ap*F/PLCL with the same dimensions served as controls. SEM examination of the cross-sections affirmed the morphology of MCS and Hollow-NGCs as designed and the electrospun sheath (214 μm and 210 μm thick, respectively) was composed of axial-oriented fibers (**Figure 4b**). As-prepared MCS-NGCs were sutured to the 10-mm rat sciatic nerve defects with 8-0 nylon suture. Macroscopic examination of grafted defects 12 weeks post-surgery revealed that the defects were successfully re-bridged without signs of inflammation (**Figure 5a**). Compared to MCS-NGCs and autografts, the hollow tubes could not maintain the shape well and kinking was seen even after 12-week implantation.

3.4. MCS-NGCs supported in vivo angiogenesis and morphogenesis of regenerated sciatic nerves

Microvessel formation within the regenerated nerve was specifically evaluated based on histologic analysis (H&E staining) and immunofluorescence staining for CD34. No sign of inflammation was observed (**Figure 5b**) and newly formed microvessels were seen in all the groups (**Figure 5c**). However, MCS-NGC and autograft showed notably higher microvessel density and diameter than Hollow-NGCs ($P < 0.01$), and no significant difference was identified between MCS and autograft groups (**Figure 5e-f**). Furthermore, immunofluorescence staining for CD34, a marker of vascular endothelial progenitor cells of microvessels, also revealed more progenitor cells in both MCS-NGC and autograft groups (**Figure 5d**).

To evaluate the nerve regeneration capacity, transverse thin sections of 12-week regenerated

nerves were stained with TB and LFB. As shown in **Figure 6a-d**, large amounts of SCs and regenerated nerve myelin were produced in all the groups. However, MCS-NGCs yielded much higher density of positive SCs and much larger area of positive myelin compared to the Hollow-NGCs ($P < 0.01$), but very similar to that of the autografts (**Figure 6b&d**). The myelination of regenerated nerves was further characterized by TEM to examine the transverse sections. While newly formed myelin sheathes were seen in all the groups (**Figure 6e**), the diameter and thickness of regenerated axons in MCS group were significantly greater than that of the hollow tube group ($P < 0.01$) and close to the autograft group (**Figure 6f**). S-100 usually plays a neurotrophic role in the peripheral nervous system and is often used as a marker for axonal growth [45]. NF-200 is an important marker of mature axons [46]. Therefore, the composition of regenerated nerves was further evaluated by immunofluorescence staining of the transverse sections for these two marker proteins. All the regenerated nerves expressed these protein markers (**Figure 6g**), but the expression levels were different: comparable levels between MCS-NGC and autograft yet significantly higher than that of Hollow-NGC groups (**Figure 6h**). This trend was further confirmed by immunohistochemical staining of GFAP protein (**Figure 6i-j**). Moreover, similar spatial distribution patterns of such proteins within the regenerated nerves were seen between MCS-NGC and autograft groups.

3.5. MCS-NGC supported functional recovery of the regenerated sciatic nerve

The gastrocnemius muscle is controlled by the sciatic nerve; thus, atrophy of the gastrocnemius muscle can serve as the indicator for functional regeneration of the sciatic nerve. Following the walking track analysis 12 weeks after surgery (**Figure 7a**), the sciatic function index (SFI) was obtained for each group. SFI of MCS-NGC group was significantly lower than that of the

Hollow-NGC group ($P < 0.01$) and close to that of autograft group (**Figure 7b**). The microstructure of TSM was then analyzed by staining the thin sections with Masson's trichrome stain (**Figure 7c**). Interestingly, much less collagen (blue regions) was formed in either MCS-NGC or autograft groups compared to the Hollow-NGC group. Quantification of the collagen amount indeed confirmed that Hollow-NGCs resulted in the highest collagen deposition ($P < 0.01$) among all three groups (**Figure 7d**) and the difference between MCS-NGC and autograft groups remained significant ($P < 0.05$), but very close, indicating a much more severe atrophy of TSM in the Hollow-NGC group than other groups. Similar trend was observed with the TSM weight ratios (**Figure 7e**), confirming that the recovery of motor functions in the MCS-NGC group was similar to that in the autograft group and significantly better than that in the Hollow-NGC group ($P < 0.05$).

4. Discussion

In view of the challenges associated with current nerve conduits, *i.e.*, exhibiting the capability of bridging the distal and proximal stumps of peripheral nerves but failing to restore the physiologic functions like autografts, this study primarily focused on the development of a biomimetic nerve conduit that could maximally resemble the architecture and morphology of nerve fascicles while recapitulating the chemical cues to guide the functional regeneration of nerve. The use of polyblend nanofibers of *Ap*F, PLCL and GO to fabricate the biomimetic MCS-NGCs yielded desired bioactivity with high porosity and interconnected micropores/microchannels, benefiting guided cell migration/ingrowth, favored cell maturation, promoted nerve regeneration. As expected, utility of such MCS-NGCs for *in vivo* regenerating sciatic nerve defects demonstrated to be effective, comparable to the autografts.

Perineurium tube is composed of collagen and elastin fibers, which can provide structural

stability and elasticity to myelin sheath [47], multifaceted advantages were identified with current MCS-NGCs, including: 1) well-preserved fibrous morphology of *Ap*F/PLCL/GO nanofibers exhibited morphological similarity to perineurium matrix; 2) *Ap*F could biologically mimic collagen as a result of the presence of RGD domains to stimulate SCs migration and proliferation as well as neurite extension; 3) incorporation of GO, favorable for migration, proliferation, and myelination of SCs ; 4) inclusion of PLCL and GO in nanofibers offers the flexibility and stability to *Ap*F [29]; and 5) introduction of parallel microchannels improved the perineurium tubular structure representation. During nerve regeneration, maintenance of the mechanical stability of NGCs is essential to protect the regenerated SCs and axon from further damage [48]. The ability of GO to improve the mechanical properties of the scaffold may come from their negative charge for repulsion [41, 49] and superficial location on the fiber surface (**Figure 1c**) to protect *Ap*F. Further efforts to understand the mechanism would be necessary.

In view of the importance of NGCs degradation in nerve regeneration, *i.e.*, the need to match with nerve regeneration rate for maintaining structural integrity while minimizing unwanted compression damage [50, 51], MCS-NGC degradation could be tuned by modulating the crosslinking degree of *Ap*F. Studies have shown that injured nerves could partially recover their function by 6 weeks [52, 53]. As such, the NGC should maintain their structural stability *in vivo* for the first 6 weeks and then degrade in a great portion afterwards [48]. In this study, MCS-NGC crosslinked with glutaraldehyde vapor for 20 min exhibited a linear degradation (**Figure S2d**), retaining 60% mass by 6 weeks and reaching 60% mass loss by two months, which partially satisfied the desirable need. If necessary, the degradation rate can be further regulated by varying the ratio between *Ap*F and PLCL or replacing PLCL with other materials.

During peripheral nerve regeneration, timely formation of the myelin sheath by SCs, the main glia cells in peripheral nerve to guide the outgrowth of axonal fibers with reciprocal interactions, is an essential step toward function recovery of regenerated nerve. In the current design, introduction of microchannels to MCS-NGCs could provide topological cues to guide the migration of SCs along the luminal surface and promote proliferation and myelinating conversion of SCs (**Figure 2c**). Promoted cell proliferation might come from the increased surface area of MCS-NGCs, providing more sites for SCs to attach (**Figure 2c**). Interestingly, culture of SCs on planar nanofiber meshes with the same composition as MCS showed reduced myelinating capacity (**Figure 3**) as confirmed by significantly elevated myelin gene expression and neurotrophin secretion in MCS. Consistent with the findings that myelinating SCs increase NGF expression while reducing NCAM [42], promoted neurotrophin secretion of NGF was measured on MCS (**Figure 3d-f**) compared to 2D nanofiber meshes, which were able to promote neuron cells (such as PC12) differentiation (**Figure 3g-i**), suggesting the regulatory role of microchannels of MCS in maturation of SCs. The exact mechanism remains elusive, however, accelerated deposition of new ECM by SCs within MCS-NGCs (**Figure 2c**, arrowheads) along with elevated secretion of NGF may primarily account for the facilitated migration of axonal fibers and potentially involve in myelination [54, 55]. Clearly, the enhanced cellular behaviors are mainly ascribed to the unique hierarchical structure of the MCS-NGCs maximally mimicking the natural fascicles [56].

Previous studies have shown that SC migration and axonal ingrowth to microchannels was not closely related to the channel diameter [57, 58]. In conjunction with optimal neovascularization [59, 60] and fabrication easiness, an average size of 125 μm was adopted, which evidently demonstrated to be effective in encouraging the regeneration of sciatic nerve with great similarity to autografts (**Figure 5-7**). Different from those microchannels with dense luminal walls [5, 18], the presence of

highly interconnected pores from fragmented nanofibers throughout the entire NGCs enabled free diffusion of nutrition, oxygen and cytokines to support the cellular functions and cell infiltration easily (**Figure 2-3**). Furthermore, the fibrous constitution of luminal surface would better mimic the morphology of the basement membrane of perineurium tube and therefore encourage SC adhesion. Indeed, all the luminal surfaces of microchannels were paved with a layer of SCs (**Figure 2c**), favoring guided axon ingrowth and myelination. In addition, the combination of multichannels and interstitial pores of fiber fragments in MCS-NGCs is even more crucial for *in vivo* implantation to assure a sufficient supply of nutrition to ingrowth nerve prior to the establishment of functional neovasculature.

During the repair of long-distance peripheral nerve defects like sciatic nerve, prompt vascularization of NGCs is essential for resolving the technical bottleneck with the lack of blood supply [61, 62], and helping guide the regeneration of peripheral nerve axons *via* reciprocal interactions between vascular endothelial cells and SCs [63, 64]. As a matter of fact, limited angiogenesis within NGCs may be considered as the major differentiator from the high success of autografts. Thus, an efficient growth-permissive microenvironment should be constructed within NGCs to achieve the desired vascularization, similar to autografts. The currently configured MCS-NGCs indeed led to the formation of neo-microvessels (both density and diameter) similar to autografts (**Figure 5d**), which in turn resulted in comparable nerve regeneration (SC density and remyelination, expression of axon maturation markers such as NF-200, and GFAP) and function recovery of the regenerated nerves (walking track, TSM morphology and weight ratio analysis) between MCS-NGCs and autografts (**Figure 6-7**). Mechanistic understanding of molecular regulation of nerve regeneration by vascularization would be necessary to achieve better axonal regeneration post peripheral nerve injury, deserving further investigation.

5. Conclusion

In this study，a biomimetic 3D NGC with parallel microchannels (~125 μm) and hierarchical architectures was fabricated from fragmented nanofibers of *Ap*F/PLCL in combination with nanomaterial GO. Such an NGC partially recapitulated the structural and compositional features of fascicles and offered an effective guiding interface for SC migration, proliferation, and myelination *in vitro* and for promoting nerve regeneration *in vivo*. With demonstrated advantages of the MCS-NGCs, further evaluation of their regenerating capacity for large size defects in other animals would provide an important framework for their potential translation especially in combination with the local delivery of potent neurotrophins.

Declaration of Competing Interest

The authors declare no competing financial interest. The manuscript was written through contributions of all authors. All authors have given approval to the final version of the manuscript.

Acknowledgement

This research was supported by National Key Research Program of China (2016YFA0201702 of 2016YFA0201700), National Nature Science Foundation of China (No.31771023), Science and Technology Commission of Shanghai Municipality (No. 19441902600), and Yantai Double Hundred Talent Plan. This was also supported by the Fundamental Research Funds for the Central Universities (Grant No. 2232019A3-07 and CUSF-DH-D-2018070) and Zhejiang Provincial Natural Science Foundation of China (LY20C100003). The authors would like to thank Tong Long (Department of radiology，RuiJin Hospital / Lu Wan Branch, School of Medicine, Shanghai

Jiaotong University) for his time and effort reviewing and revising this manuscript.

Reference

[1] D. Xu, L. Fan, L. Gao, Y. Xiong, Y. Wang, Q. Ye, A.X. Yu, H. Dai, Y. Yin, J. Cai, Micro-nano-structured Polyaniline Assembled in Cellulose Matrix Via Interfacial Polymerization for Applications in Nerve Regeneration, ACS Appl. Mater. Interfaces 8(27) (2016) 17090-17097.

[2] C. Ide, K. Tohyama, K. Tajima, K. Endoh, K. Sano, M. Tamura, A. Mizoguchi, M. Kitada, T. Morihara, M. Shirasu, Long acellular nerve transplants for allogeneic grafting and the effects of basic fibroblast growth factor on the growth of regenerating axons in dogs: a preliminary report, Exp Neuol 154(1) (1998) 99-112.

[3] X. Yu, R.V. Bellamkonda, Tissue-engineered scaffolds are effective alternatives to autografts for bridging peripheral nerve gaps, Tissue Eng 9(3) (2003) 421-430.

[4] X. Gu, F. Ding, Y. Yang, J. Liu, Construction of tissue engineered nerve grafts and their application in peripheral nerve regeneration, Prog. Neurobiol. 93(2) (2011) 204-230.

[5] G.C. de Ruiter, R.J. Spinner, M.J. Malessy, M.J. Moore, E.J. Sorenson, B.L. Currier, M.J. Yaszemski, A.J. Windebank, Accuracy of motor axon regeneration across autograft, single-lumen, and multichannel poly(lactic-co-glycolic acid) nerve tubes, Neurosurgery 63(1) (2008) 144-155.

[6] H. Xueyu, H. Jinghui, Y. Zhengxu, X. Lei, L. Mo, L. Bochang, S. Xuefeng, L. Zhuojing, A novel scaffold with longitudinally oriented microchannels promotes peripheral nerve regeneration, Tissue Eng Part A 15(11) (2009) 3297-3308.

[7] T.M. Brushart, M.V. Mathur, M.R. Sood, G.M. Koschorke, Dispersion of regenerating axons across enclosed neural gaps **, J. Hand Surg. 20(4) (1995) 557–564.

[8] N. Dubey, P.C. Letourneau, R.T. Tranquillo, Guided Neurite Elongation and Schwann Cell Invasion into Magnetically Aligned Collagen in Simulated Peripheral Nerve Regeneration, Exp Neuol 158(2) (1999) 338-350.

[9] K. Matsumoto, K. Ohnishi, T. Kiyotani, T. Sekine, H. Ueda, T. Nakamura, K. Endo, Y. Shimizu, Peripheral nerve regeneration across an 80-mm gap bridged by a polyglycolic acid (PGA)–collagen tube filled with laminin-coated collagen fibers: a histological and electrophysiological evaluation of regenerated nerves, Brain Res. 868(2) (2000) 315-328.

[10] J. Cai, X. Peng, K.D. Nelson, R. Eberhart, G.M. Smith, Permeable guidance channels containing microfilament scaffolds enhance axon growth and maturation, J. Biomed. Mater. Res. A 75A(2) (2010) 374-386.

[11] S.Y. Chew, R. Mi, A. Hoke, K.W. Leong, Aligned Protein-Polymer Composite Fibers Enhance

Nerve Regeneration: A Potential Tissue-Engineering Platform, Adv. Funct. Mater. 17(8) (2010) 1288-1296.

[12] G. Xiaosong, D. Fei, D.F. Williams, Neural tissue engineering options for peripheral nerve regeneration, Biomaterials 35(24) (2014) 6143-6156.

[13] E.C. Spivey, Z.Z. Khaing, J.B. Shear, C.E. Schmidt, The fundamental role of subcellular topography in peripheral nerve repair therapies, Biomaterials 33(17) (2012) 4264-4276.

[14] D. Fozdar, J. Lee, C. Schmidt, S. Chen, Hippocampal neurons respond uniquely to topographies of various sizes and shapes, Biofabrication 2(3) (2010) 035005.

[15] L. Yao, K.L. Billiar, A.J. Windebank, A. Pandit, Multichanneled collagen conduits for peripheral nerve regeneration: design, fabrication, and characterization, Tissue Eng Part C Methods 16(6) (2010) 1585-1596.

[16] X. Wang, W. Hu, Y. Cao, J. Yao, J. Wu, X. Gu, Dog sciatic nerve regeneration across a 30-mm defect bridged by a chitosan/PGA artificial nerve graft, Brain 128(Pt 8) (2005) 1897-1910.

[17] S. Wang, L. Cai, Polymers for Fabricating Nerve Conduits, Int J Polym Sci. (2010).

[18] V. Chiono, C. Tonda-Turo, Trends in the design of nerve guidance channels in peripheral nerve tissue engineering, Prog. Neurobiol. 131 (2015) 87-104.

[19] J.D. Stewart, Peripheral nerve fascicles: anatomy and clinical relevance, Muscle Nerve 28(5) (2010) 525-541.

[20] T.M. Dinis, R. Elia, G. Vidal, Q. Dermigny, C. Denoeud, D.L. Kaplan, C. Egles, F. Marin, 3D multi-channel bi-functionalized silk electrospun conduits for peripheral nerve regeneration, J Mech Behav Biomed Mater 41 (2015) 43-55.

[21] X. Jingwei, S.M. Willerth, L. Xiaoran, M.R. Macewan, R. Allison, S.E. Sakiyama-Elbert, X. Younan, The differentiation of embryonic stem cells seeded on electrospun nanofibers into neural lineages, Biomaterials 30(3) (2009) 354-362.

[22] G.T. Christopherson, H. Song, H.Q. Mao, The influence of fiber diameter of electrospun substrates on neural stem cell differentiation and proliferation, Biomaterials 30(4) (2009) 556-564.

[23] X. Jingwei, M.R. Macewan, A.G. Schwartz, X. Younan, Electrospun nanofibers for neural tissue engineering, Nanoscale 2(1) (2010) 35-44.

[24] K. Wang, M. Xu, M. Zhu, H. Su, H. Wang, D. Kong, L. Wang, Creation of macropores in electrospun silk fibroin scaffolds using sacrificial PEO-microparticles to enhance cellular infiltration, J. Biomed. Mater. Res. A 101(12) (2013) 3474-3481.

[25] T. Xu, J.M. Miszuk, Y. Zhao, H. Sun, H. Fong, Electrospun Polycaprolactone 3D Nanofibrous

Scaffold with Interconnected and Hierarchically Structured Pores for Bone Tissue Engineering, Adv Healthc Mater 4(15) (2015) 2238-2246.

[26] W. Chen, S. Chen, Y. Morsi, H. El-Hamshary, M. El-Newhy, C. Fan, X. Mo, Superabsorbent 3D Scaffold Based on Electrospun Nanofibers for Cartilage Tissue Engineering, ACS Appl. Mater. Interfaces 8(37) (2016) 24415-24425.

[27] B. Sun, Z.F. Zhou, T. Wu, W. Chen, D. Li, H. Zheng, H. El-Hamshary, S.S. Al-Deyab, X. Mo, Y. Yu, Development of Nanofiber Sponges-Containing Nerve Guidance Conduit for Peripheral Nerve Regeneration in Vivo, ACS Appl. Mater. Interfaces 9(32) (2017) 26684-26696.

[28] G.C.D. Ruiter, O.E.T. Liang, Methods for in vitro characterization of multichannel nerve tubes, J. Biomed. Mater. Res. A 84A(3) (2010) 643-651.

[29] J. Wang, B. Sun, M.A. Bhutto, T. Zhu, Y.U. Kui, J. Bao, Y. Morsi, H. Elhamshary, M. Elnewehy, M.O. Xiumei, Fabrication and characterization of Antheraea pernyi silk fibroin-blended P(LLA-CL) nanofibrous scaffolds for peripheral nerve tissue engineering, Front. Mater. Sci 11 (2017) 22-32.

[30] J. Wang, Y. Cheng, L. Chen, T. Zhu, K. Ye, C. Jia, H. Wang, M. Zhu, C. Fan, X. Mo, In vitro and in vivo studies of electroactive reduced graphene oxide-modified nanofiber scaffolds for peripheral nerve regeneration, Acta Biomater. 84 (2019) 98-113.

[31] K. Zhang, H. Zheng, S. Liang, C. Gao, Aligned PLLA nanofibrous scaffolds coated with graphene oxide for promoting neural cell growth, Acta Biomater. 37 (2016) 131-142.

[32] J. Song, H. Gao, G. Zhu, X. Cao, X. Shi, Y. Wang, The preparation and characterization of polycaprolactone/graphene oxide biocomposite nanofiber scaffolds and their application for directing cell behaviors, Carbon 95 (2015) 1039-1050.

[33] Y. Qian, J. Song, X. Zhao, W. Chen, Y. Ouyang, W. Yuan, C. Fan, 3D Fabrication with Integration Molding of a Graphene Oxide/Polycaprolactone Nanoscaffold for Neurite Regeneration and Angiogenesis, Adv. Sci. 5(4) (2018) 1700499-1700517.

[34] J. Wang, S. Zhang, T. Xing, B. Kundu, M. Li, S.C. Kundu, S. Lu, Ion-induced fabrication of silk fibroin nanoparticles from Chinese oak tasar Antheraea pernyi, Int. J. Biol. Macromol. 79 (2015) 316-325.

[35] I.R. Serra, R. Fradique, M.C.S. Vallejo, T.R. Correia, S.P. Miguel, I.J. Correia, Production and characterization of chitosan/gelatin/β-TCP scaffolds for improved bone tissue regeneration, Mater. Sci. Eng. C 55 (2015) 592-604.

[36] J. Huang, X. Hu, L. Lu, Z. Ye, Q. Zhang, Z. Luo, Electrical regulation of Schwann cells using conductive polypyrrole/chitosan polymers, J. Biomed. Mater. Res. A 93(1) (2010) 164-174.

[37] M.L. De, W.J. Freed, R.J. Wyatt, An index of the functional condition of rat sciatic nerve based

on measurements made from walking tracks, Exp Neurol. 77(3) (1982) 634-643.

[38] Y. Luo, H. Shen, Y. Fang, Y. Cao, J. Huang, M. Zhang, J. Dai, X. Shi, Z. Zhang, Enhanced proliferation and osteogenic differentiation of mesenchymal stem cells on graphene oxide-incorporated electrospun poly (lactic-co-glycolic acid) nanofibrous mats, ACS Appl. Mater. Interfaces 7(11) (2015) 6331-6339.

[39] S. Roy, N. Soin, R. Bajpai, D.S. Misra, J.A. Mclaughlin, S.S. Roy, Graphene oxide for electrochemical sensing applications, J. Mater. Chem. 21(38) (2011) 14725-14731.

[40] J. Zhang, H. Yang, G. Shen, P. Cheng, J. Zhang, S. Guo, Reduction of graphene oxide via L-ascorbic acid, Chem Commun 46(7) (2010) 1112-1114.

[41] J. Wang, Z. Yin, X. Xue, S. Kundu, X. Mo, S. Lu, Natural Non-Mulberry Silk Nanoparticles for Potential-Controlled Drug Release, Int. J. Mol. Sci 17(12) (2016) 2012-2027.

[42] W. Fei, Y. Aixi, X. Danmou, K. Wusheng, P. Zhengren, R. Ting, The mood stabilizer valproic acid induces proliferation and myelination of rat Schwann cells, Neurosci. Res. 70(4) (2011) 383-390.

[43] J.S. Belkas, M.S. Shoichet, R. Midha, Peripheral nerve regeneration through guidance tubes, Neurol. Res 26(2) (2004) 151-160.

[44] Y. Wu, L. Wang, B. Guo, Y. Shao, P.X. Ma, Electroactive biodegradable polyurethane significantly enhanced Schwann cells myelin gene expression and neurotrophin secretion for peripheral nerve tissue engineering, Biomaterials 87 (2016) 18-31.

[45] D.M. Mata, D. Alessi, D.J. Fink, S100 is preferentially distributed in myelin-forming Schwann cells, Journal of Neurocytology 19(3) (1990) 432-442.

[46] R. Posmantur, R.L. Hayes, C.E. Dixon, W.C. Taft, Neurofilament 68 and neurofilament 200 protein levels decrease after traumatic brain injury, Journal of Neurotrauma 11(5) (1994) 533.

[47] G.-H. Han, J. Peng, P. Liu, X. Ding, S. Wei, S. Lu, Y. Wang, Therapeutic strategies for peripheral nerve injury: decellularized nerve conduits and Schwann cell transplantation, Neural Regen. Res. 14(8) (2019) 1343-1351.

[48] G.-W. Wang, H. Yang, W.-F. Wu, P. Zhang, J.-Y. Wang, Design and optimization of a biodegradable porous zein conduit using microtubes as a guide for rat sciatic nerve defect repair, Biomaterials 131 (2017) 145-159.

[49] H. Bai, C. Li, X. Wang, G. Shi, A pH-sensitive graphene oxide composite hydrogel, Chem Commun 46(14) (2010) 2376-2378.

[50] P. Moroder, M.B. Runge, H. Wang, T. Ruesink, L. Lu, R.J. Spinner, A.J. Windebank, M.J. Yaszemski, Material properties and electrical stimulation regimens of polycaprolactone fumarate–

polypyrrole scaffolds as potential conductive nerve conduits, Acta Biomater. 7(3) (2011) 944-953.

[51] D.J. Lee, A. Fontaine, X. Meng, D. Park, Biomimetic nerve guidance conduit containing intraluminal microchannels with aligned nanofibers markedly facilitates in nerve regeneration, ACS Biomater Sci Eng 2(8) (2016) 1403-1410.

[52] Y.-S. Chen, J.-Y. Chang, C.-Y. Cheng, F.-J. Tsai, C.-H. Yao, B.-S. Liu, An in vivo evaluation of a biodegradable genipin-cross-linked gelatin peripheral nerve guide conduit material, Biomaterials 26(18) (2005) 3911-3918.

[53] Y.-Y. Hsueh, Y.-J. Chang, T.-C. Huang, S.-C. Fan, D.-H. Wang, J.-J.J. Chen, C.-C. Wu, S.-C. Lin, Functional recoveries of sciatic nerve regeneration by combining chitosan-coated conduit and neurosphere cells induced from adipose-derived stem cells, Biomaterials 35(7) (2014) 2234-2244.

[54] S.P. Frostick, Q. Yin, G.J. Kemp, Schwann cells, neurotrophic factors, and peripheral nerve regeneration, Microsurgery 18(7) (1998) 397-405.

[55] J.R. Chan, J.M. Cosgaya, Y.J. Wu, E.M. Shooter, Neurotrophins are key mediators of the myelination program in the peripheral nervous system, Proc. Natl. Acad. Sci. U.S.A. 98(25) (2001) 14661-14668.

[56] P.A. Wieringa, A.R. Gonçalves de Pinho, S. Micera, R.J. van Wezel, L. Moroni, Biomimetic architectures for peripheral nerve repair: a review of biofabrication strategies, Adv Healthc Mater 7(8) (2018) 1701164-1701183.

[57] J.B. Scott, M. Afshari, R. Kotek, J.M. Saul, The promotion of axon extension in vitro using polymer-templated fibrin scaffolds, Biomaterials 32(21) (2011) 4830-4839.

[58] W. Daly, L. Yao, D. Zeugolis, A. Windebank, A. Pandit, A biomaterials approach to peripheral nerve regeneration: bridging the peripheral nerve gap and enhancing functional recovery, J. Royal Soc. Interface 9(67) (2011) 202-221.

[59] X. Xiao, W. Wang, D. Liu, H. Zhang, P. Gao, L. Geng, Y. Yuan, J. Lu, Z. Wang, The promotion of angiogenesis induced by three-dimensional porous beta-tricalcium phosphate scaffold with different interconnection sizes via activation of PI3K/Akt pathways, Sci Rep. 5 (2015) 9409-9418.

[60] Y.-C. Chiu, M.-H. Cheng, H. Engel, S.-W. Kao, J.C. Larson, S. Gupta, E.M. Brey, The role of pore size on vascularization and tissue remodeling in PEG hydrogels, Biomaterials 32(26) (2011) 6045-6051.

[61] R.K. Jain, P. Au, J. Tam, D.G. Duda, D. Fukumura, Engineering vascularized tissue, Nat Biotechnol. 23(7) (2005) 821-823.

[62] E.C. Novosel, C. Kleinhans, P.J. Kluger, Vascularization is the key challenge in tissue engineering, Adv Drug Deliv Rev 63(4-5) (2011) 300-311.

[63] H. Wang, H. Zhu, Q. Guo, T. Qian, P. Zhang, S. Li, C. Xue, X. Gu, Overlapping mechanisms of peripheral nerve regeneration and angiogenesis following sciatic nerve transection, Front Cell Neurosci. 11 (2017) 323-336.

[64] A.-L. Cattin, J.J. Burden, L. Van Emmenis, F.E. Mackenzie, J.J. Hoving, N.G. Calavia, Y. Guo, M. McLaughlin, L.H. Rosenberg, V. Quereda, Macrophage-induced blood vessels guide Schwann cell-mediated regeneration of peripheral nerves, Cell 162(5) (2015) 1127-1139.

Figure captions

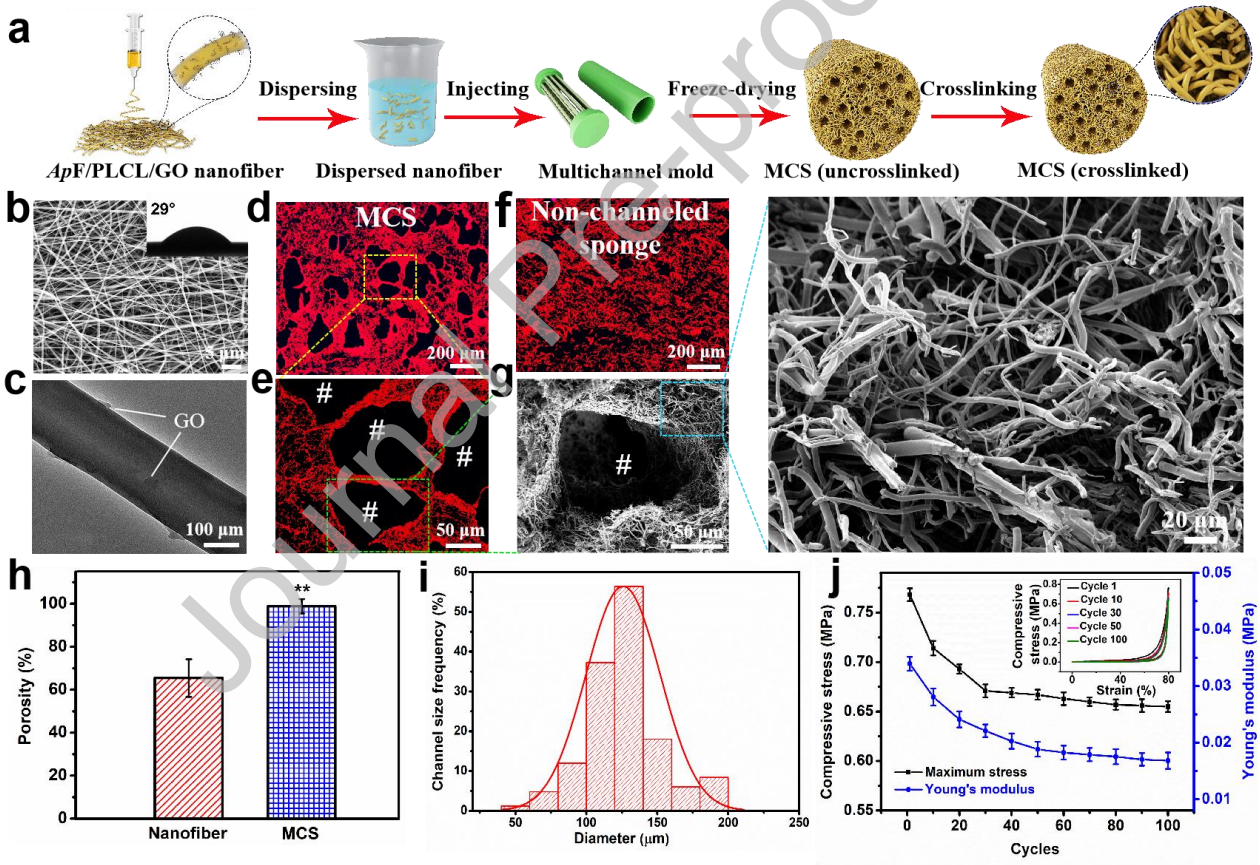

Figure 1. Characterization of MCS fabricated from *Ap*F/PLCL/GO nanofibers. (a) Schematic illustration of the key procedures in fabrication of MCS; (b) SEM image of *Ap*F/PLCL/GO nanofibers. Inset: apparent contact angle of *Ap*F/PLCL/GO nanofibers; (c) Transmission electron microscopy (TEM) images of *Ap*F/PLCL/GO nanofiber, the lines indicate the GO nanosheets. (d) Fluorescence micrographs of 3D MCS (Inset: transverse fluorescence micrograph of MCS) and (e) high magnification of selected region. (f) Fluorescence micrographs of no-channeled sponge. (g) Scanning electron microscopy (SEM) image of 3D MCS in the selected region in (e) and high magnification of selected region. (h) Porosity of 2D nanofibers

and 3D MCS (** P < 0.01), and (i) channel size distribution of 3D MCS. (j) Compressive mechanical properties of 3D MCS. Inset of (j) is compressive stress-strain curves of 3D MCS with different cycles.

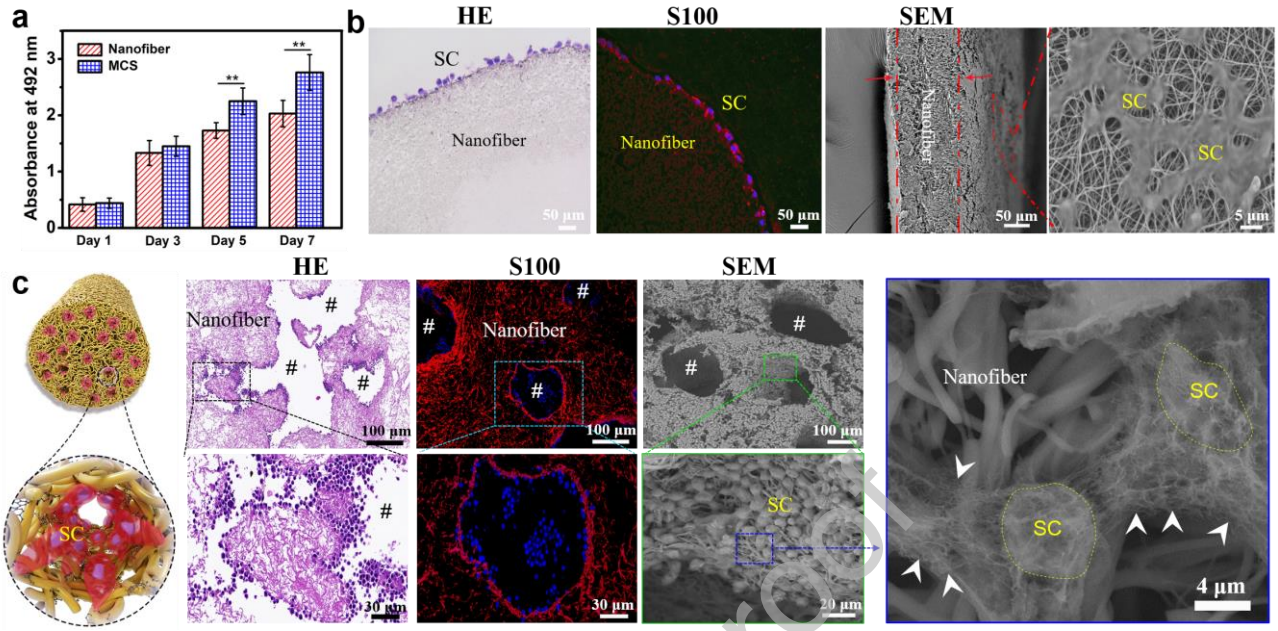

Figure 2. SC proliferation and spatial distribution on nanofibers and within MCS. (a) Proliferation of SCs cultured on *Ap*F/PLCL/GO nanofiber mesh or MCS for 1, 3, 5 and 7 d, (** P < 0.01). (b) Images of SCs cultured on nanofiber mesh for 7 days, characterized by H&E staining, immunofluorescence staining and SEM of the transverse sections. (c) Images of SCs cultured within MCS for 7 days, characterized by H&E staining, immunofluorescence staining and SEM. Cytoplasm was stained by S100 (red) and nuclei were stained by DAPI (blue). # denotes the microchannels. Arrowheads indicate the new ECM secreted by SCs.

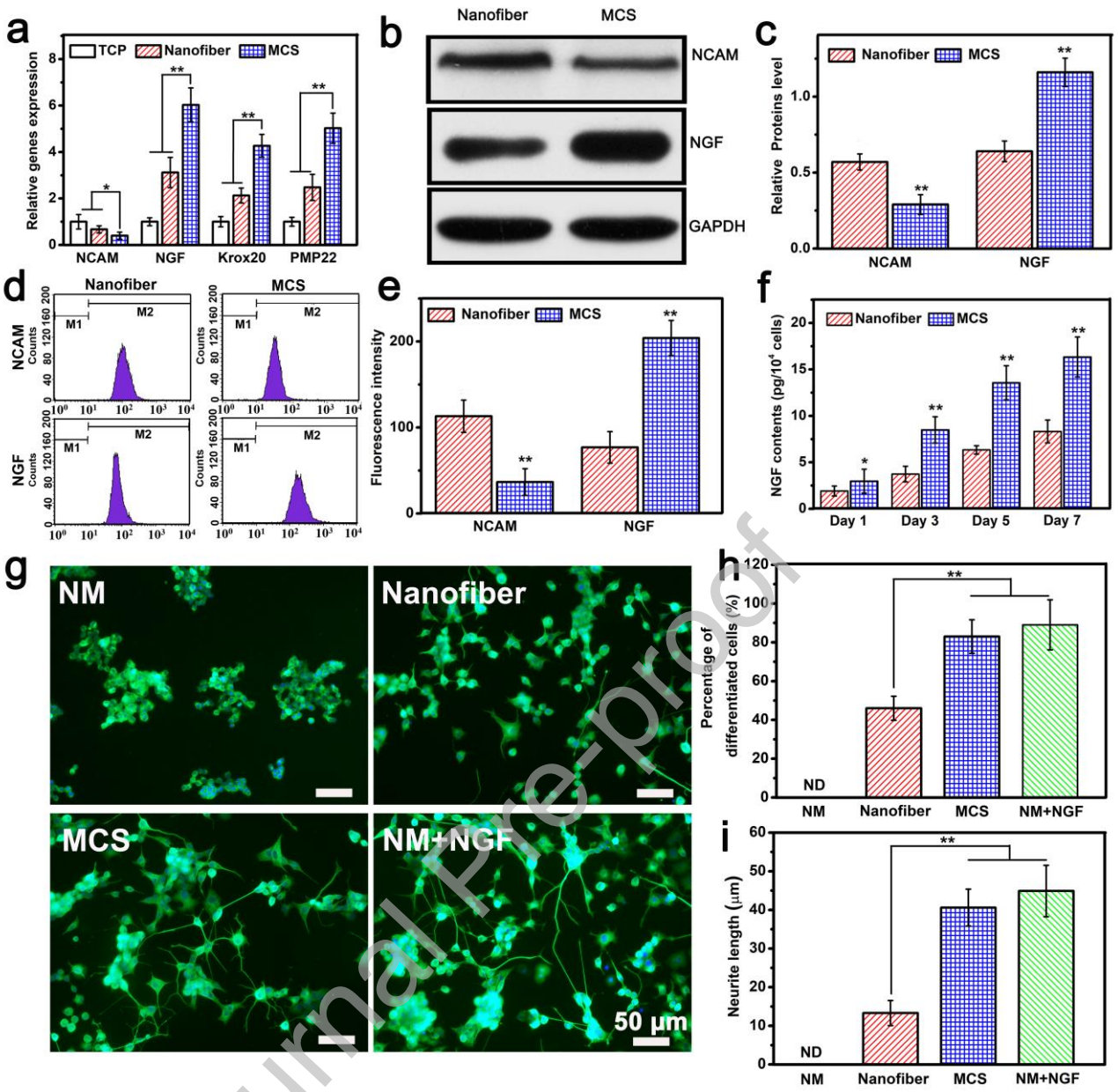

Figure 3. Myelination of SCs cultured on nanofiber mesh and MCS. (a) Gene expression as determined by qRT-PCR; (b) Western blot and (c) semi-quantification of protein levels of NCAM and NGF; (d) Flow cytometry and (e) corresponding fluorescence intensity of NCAM and NGF protein expression. (f) Quantification of NGF protein in the supernatant of SCs. **(g)** PC12 cell differentiation induced by the conditioned media of SCs cultured on various scaffolds and quantitative analysis of percentage of differentiated PC12 cells (h) and neurite length (i) for each group, * $P < 0.05$, ** $P < 0.01$. NM=Normal media.

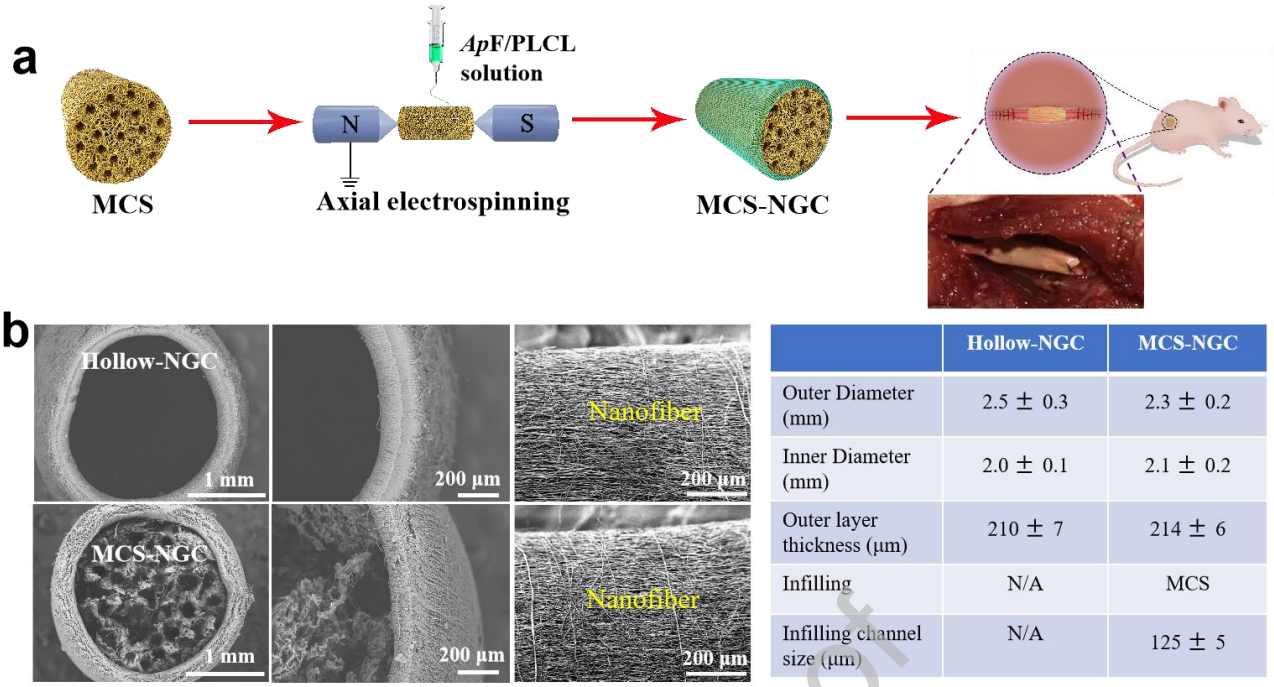

	Hollow-NGC	MCS-NGC
Outer Diameter (mm)	2.5 ± 0.3	2.3 ± 0.2
Inner Diameter (mm)	2.0 ± 0.1	2.1 ± 0.2
Outer layer thickness (μm)	210 ± 7	214 ± 6
Infilling	N/A	MCS
Infilling channel size (μm)	N/A	125 ± 5

Figure 4. Fabrication and implantation of MCS-NGC for sciatic nerve repair. (a) Schematic illustration of the fabrication of MCS-NGC and photograph of the implanted nerve conduits. (b) SEM images of the inner and outer of MCS-NGC and Hollow-NGC. The key features are listed in the table.

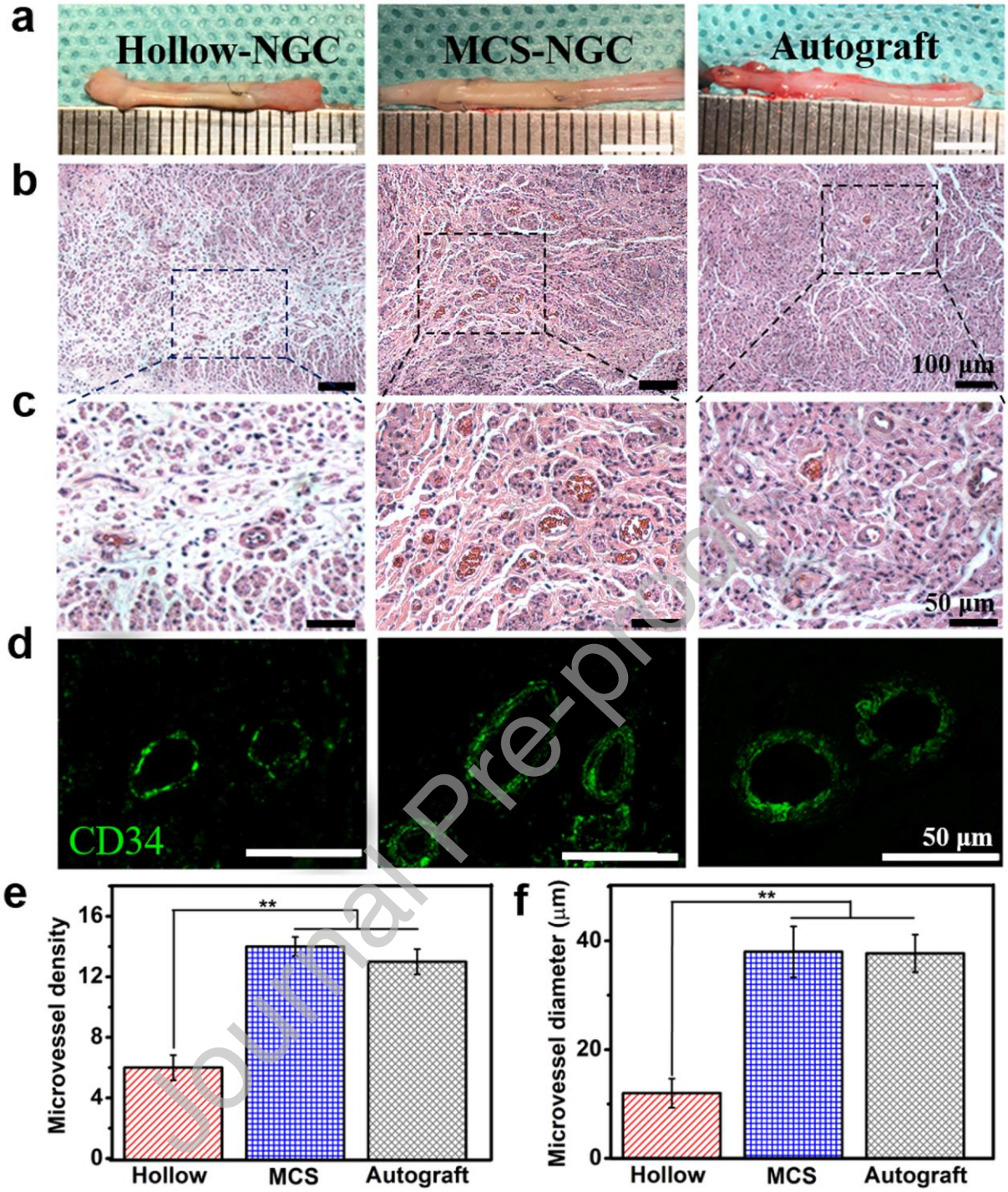

Figure 5. The general observation of regenerated nerve tissue and angiogenesis evaluation in sciatic nerve regeneration at 12 weeks postoperatively. (a) Photographs of the regenerated nerves by various grafts. (b, c) Optical images of the transverse sections of regenerated nerve tissue after H&E staining. (d) Images of the transverse sections of the middle portion of regenerated nerves, immune-fluorescently stained for CD34. (e) Density and (f) diameter of newly formed microvessels based on H&E stained sections. (** $P < 0.01$).

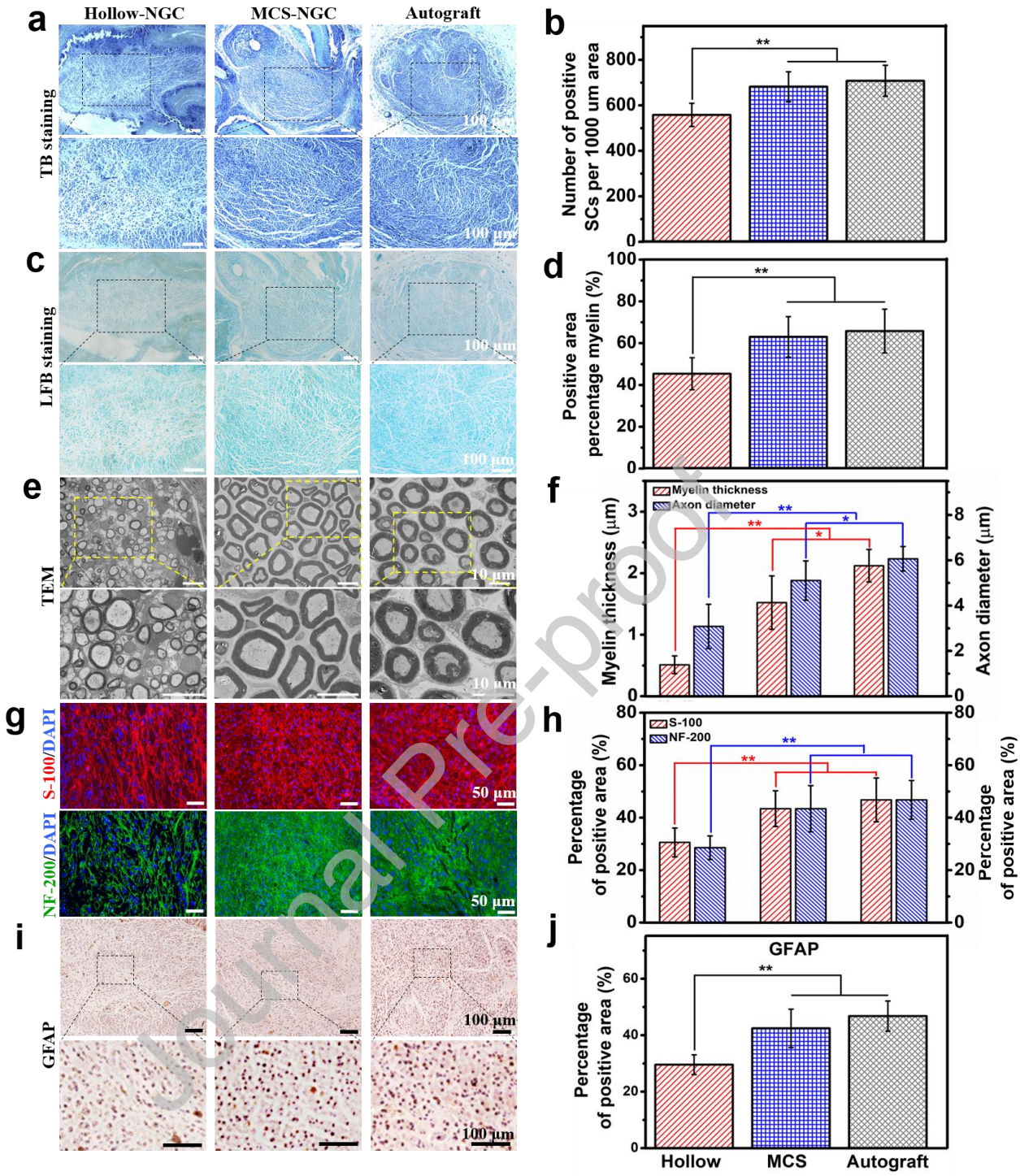

Figure 6. Morphological and structural analysis of regenerated nerve 12-week postimplantation. (a) Optical images of TB staining and (b) the corresponding density of SC; (c) Optical images of LFB staining and (d) the percentage of positive myelin area; (e) TEM micrographs of the regenerated nerve and calculated (f) axon diameter and myelin thickness; (g) Images of immunofluorescence staining of S-100 and NF-200 and the quantification for relative positive area of (h) S-100 and NF-200; (i) Images of immunohistochemical staining for GFAP and the quantification for relative positive area of (j) GFAP, (* $P < 0.05$ and ** $P < 0.01$).

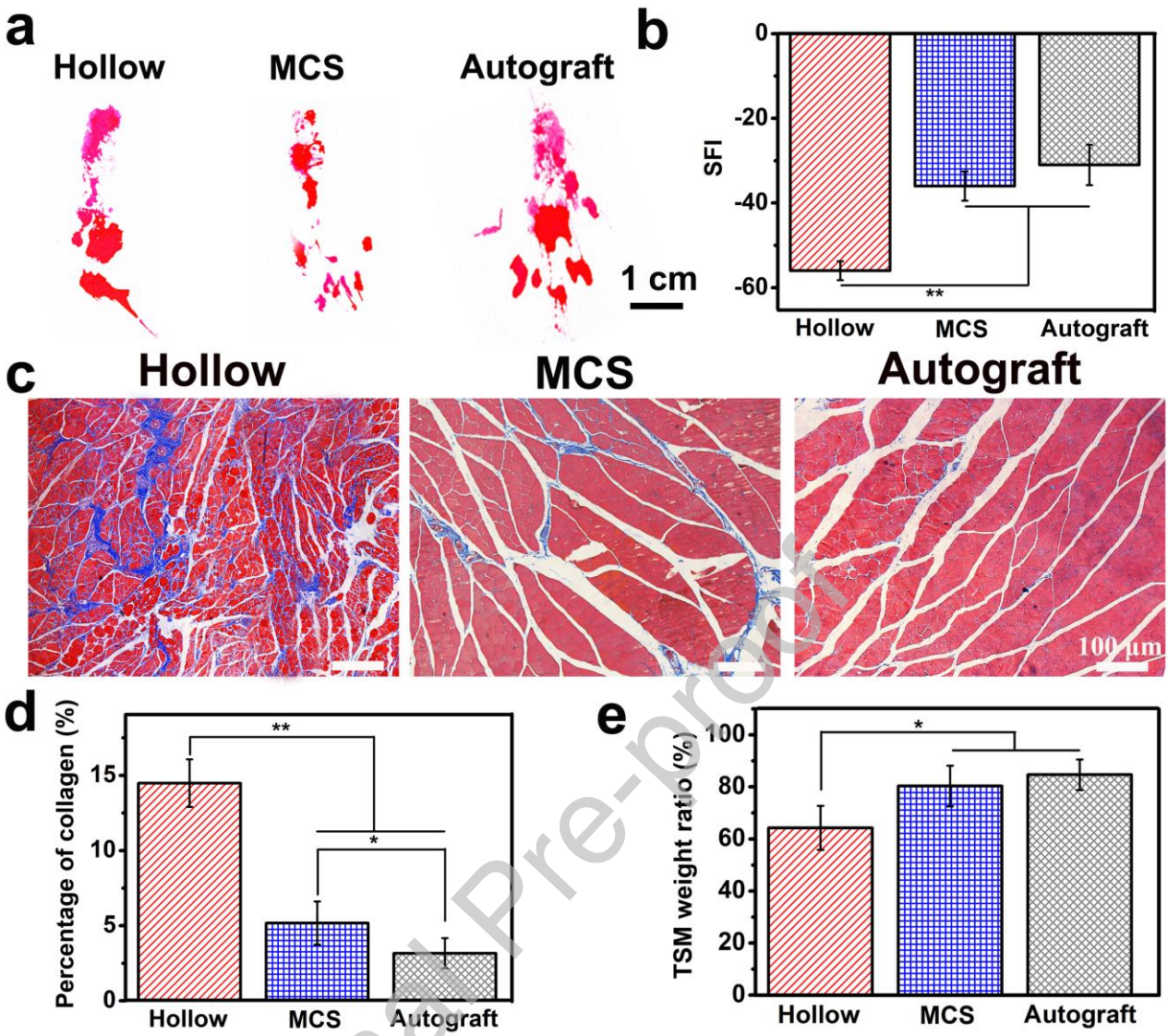

Figure 7. Functional analysis of the regenerated nerve 12-week postimplantation. (a) Walking track analysis of the experimental rats. (b) SFI calculated from the walking track. (c) Optical images of Masson trichrome stained TSMs and (d) the statistical results of percentage of collagen. (e) TSM weight ratio analysis, * $P < 0.05$ and ** $P < 0.01$.

Biomimetic and Hierarchical Nerve Conduits from Multifunctional Nanofibers for Guided Peripheral Nerve Regeneration